



LJMU Research Online

Foley, RJ, Perley, DA, Pooley, D, Prochaska, JX, Bloom, JS, Li, W, Cobb, B, Chen, HW, Aldering, G, Bailyn, C, Blake, CH, Falco, EE, Green, PJ, Kowalski, MP, Perlmutter, S, Roth, K and Volk, K

GRB 050408: A bright gamma-ray burst probing an atypical galactic environment

<http://researchonline.ljmu.ac.uk/id/eprint/6451/>

Article

Citation (please note it is advisable to refer to the publisher's version if you intend to cite from this work)

Foley, RJ, Perley, DA, Pooley, D, Prochaska, JX, Bloom, JS, Li, W, Cobb, B, Chen, HW, Aldering, G, Bailyn, C, Blake, CH, Falco, EE, Green, PJ, Kowalski, MP, Perlmutter, S, Roth, K and Volk, K (2006) GRB 050408: A bright gamma-ray burst probing an atypical galactic environment. The Astrophysical

LJMU has developed **LJMU Research Online** for users to access the research output of the University more effectively. Copyright © and Moral Rights for the papers on this site are retained by the individual authors and/or other copyright owners. Users may download and/or print one copy of any article(s) in LJMU Research Online to facilitate their private study or for non-commercial research. You may not engage in further distribution of the material or use it for any profit-making activities or any commercial gain.

The version presented here may differ from the published version or from the version of the record. Please see the repository URL above for details on accessing the published version and note that access may require a subscription.

For more information please contact researchonline@ljmu.ac.uk

<http://researchonline.ljmu.ac.uk/>

GRB 050408: A BRIGHT GAMMA-RAY BURST PROBING AN ATYPICAL GALACTIC ENVIRONMENT

R. J. FOLEY,¹ D. A. PERLEY,¹ D. POOLEY,^{1,2} J. X. PROCHASKA,³ J. S. BLOOM,¹ W. LI,¹ B. COBB,⁴
H.-W. CHEN,⁵ G. ALDERING,⁶ C. BAILYN,⁴ C. H. BLAKE,⁷ E. E. FALCO,⁸ P. J. GREEN,⁷
M. P. KOWALSKI,⁶ S. PERLMUTTER,⁶ K. ROTH,⁹ AND K. VOLK⁹

Received 2005 December 4; accepted 2006 March 11

ABSTRACT

The bright GRB 050408 was localized by *HETE-2* near local midnight in the Western Hemisphere, enabling an impressive ground-based follow-up effort, as well as space-based follow-up from *Swift*. The *Swift* data from the XRT and our own optical photometry and spectrum of the afterglow provide the cornerstone for our analysis. Under the traditional assumption that the visible wave band was above the peak synchrotron frequency and below the cooling frequency, the optical photometry of 0.03–5.03 days shows an afterglow decay corresponding to an electron energy index of $p_{lc} = 2.05 \pm 0.04$, without a jet break as suggested by others. A break is seen in the X-ray data at early times (at $\sim 12,600$ s after the GRB). The spectral slope of the optical spectrum is consistent with p_{lc} assuming a host galaxy extinction of $A_V = 1.18$ mag. The optical-NIR broadband spectrum is also consistent with $p = 2.05$ but prefers $A_V = 0.57$ mag. The X-ray afterglow shows a break at 1.26×10^4 s, which may be the result of a refreshed shock. This burst stands out in that the optical and X-ray data suggest a large H I column density of $N_{H1} \approx 10^{22}$ cm⁻²; it is very likely a damped Ly α system, so the faintness of the host galaxy ($M_V > -18$ mag) is noteworthy. Moreover, we detect extraordinarily strong Ti II absorption lines with a column density through the GRB host that exceeds the largest values observed for the Milky Way by 1 order of magnitude. Furthermore, the Ti II equivalent width is in the top 1% of Mg II absorption-selected QSOs. This suggests that the large-scale environment of GRB 050408 has significantly lower Ti depletion than our Galaxy and a large velocity width ($\delta v > 150$ km s⁻¹).

Subject headings: galaxies: ISM — galaxies: photometry — gamma rays: bursts — stars: formation

1. INTRODUCTION

Leading up to the launch of *Swift* (Gehrels et al. 2004), the astronomical community prepared for massive, multiwavelength studies of gamma-ray bursts (GRBs) expected from the satellite. Not long after the launch of *Swift*, *HETE-2* (Sakamoto et al. 2005) detected GRB 050408 (trigger H3711) at 16:22:50.93 on 2005 April 8 (UT dates are used throughout this paper). Soon after its detection, *Swift* triggered a Target of Opportunity on the GRB (Wells et al. 2005). Later, a fading optical afterglow was detected (de Ugarte Postigo et al. 2005), and a redshift of $z \approx 1.236$ was obtained through host galaxy emission lines and afterglow absorption features (Berger et al. 2005; Prochaska et al. 2005a). Radio observations were also obtained, but no transient was found (Soderberg 2005). The X-ray afterglow (Wells et al. 2005) was observed over several epochs with *Swift*, leading to an initial inference of a break (Godet et al. 2005), which was later retracted (Capalbi et al. 2005). Finally, with all the X-Ray Telescope (XRT)

data, the *Swift* team suggested a jet break at $t_{\text{break}} = (1.2 \pm 0.5) \times 10^5$ s after the GRB trigger (Covino et al. 2005).

We present light curves of the optical, infrared, and X-ray afterglows in §§ 2 and 3. A detailed analysis of these afterglows is presented in § 4. An analysis of the optical and X-ray afterglow spectra is presented in §§ 3 and 5. From the absorption in these spectra we are able to place lower limits on the metallicity and the hydrogen column of the host galaxy. Throughout the paper, the concordance cosmology of $\Omega_\Lambda = 0.71$, $\Omega_m = 0.29$, and $H_0 = 71$ km s⁻¹ Mpc⁻¹ is used. Although all measurements reported herein are consistent with our preliminary reports in the GRB Coordinates Network (GCN) Circulars, these measurements supersede those in the Circulars.

2. THE OPTICAL-INFRARED AFTERGLOW

At approximately 18:50 on 2005 April 8, 2.4 hr after the burst, de Ugarte Postigo et al. (2005) detected the optical afterglow of GRB 050408. From this time until 20:10 on April 13, the afterglow was monitored, with many groups reporting preliminary magnitudes and upper limits in the GCN Circulars.¹⁰ Here we report observations from the Keck and Magellan telescopes and perform our own reductions of the *Swift* Ultraviolet/Optical Telescope (UVOT) data, as described below. All observations are summarized in Table 3.

2.1. Magellan Optical Imaging

Our imaging with the IMACS instrument (Bigelow et al. 1998) on the Magellan I 6.5 m (Baade) Telescope began at 00:12 on 2005 April 9, about 470 minutes after the burst. Two 180 s exposures of the burst field were taken with the R_c filter and three 180 s exposures with the I_c filter. Images were reduced in the standard manner using dome flats acquired on the night of the

¹ Department of Astronomy, University of California, Berkeley, CA 94720-3411; rfoley@astro.berkeley.edu, dperley@astro.berkeley.edu, dave@astro.berkeley.edu, jbloome@astro.berkeley.edu, weidong@astro.berkeley.edu.

² Chandra Fellow.

³ UCO/Lick Observatory, University of California, Santa Cruz, 1156 High Street, Santa Cruz, CA 95064; xavier@ucolick.org.

⁴ Department of Astronomy, Yale University, P.O. Box 208101, New Haven, CT 06520; cobb@astro.yale.edu, baily@astro.yale.edu.

⁵ Department of Astronomy, University of Chicago, 5640 South Ellis Avenue, Chicago, IL 60637; hchen@oddjob.uchicago.edu.

⁶ E. O. Lawrence Berkeley National Laboratory, 1 Cyclotron Road, Berkeley, CA 94720; galdering@lbl.gov, mpkowsk@lbl.gov, saul@lbl.gov.

⁷ Harvard-Smithsonian Center for Astrophysics, 60 Garden Street, Cambridge, MA 02138; cblake@cfa.harvard.edu, pgreen@head.cfa.harvard.edu.

⁸ F. L. Whipple Observatory, Smithsonian Institution, P.O. Box 6369, Amado, AZ 85645; falco@cfa.harvard.edu.

⁹ Gemini Observatory, 670 North A'ohoku Place, Hilo, HI 96720; kroth@gemini.edu, kvolk@gemini.edu.

¹⁰ See <http://gcn.gsfc.nasa.gov/>.

TABLE 1
SDSS REFERENCE STARS

SDSS ObsID	R.A. (deg)	Decl. (deg)	g' (mag)	r' (mag)	i' (mag)	Images Applied to
587734893827063893.....	180.50328	10.804996	18.935 ± 0.010	17.583 ± 0.006	16.952 ± 0.005	M ^a
587732772665294967.....	180.53813	10.823279	18.827 ± 0.008	18.370 ± 0.007	18.208 ± 0.008	M
587732772665294873.....	180.54322	10.860261	18.944 ± 0.009	18.601 ± 0.008	18.474 ± 0.010	M, K ^b
587734893827129348.....	180.55899	10.783250	17.741 ± 0.005	17.412 ± 0.005	17.280 ± 0.006	M
587732772665294997.....	180.59562	10.899296	18.796 ± 0.008	18.484 ± 0.008	18.377 ± 0.009	K
587732772665295483.....	180.58477	10.862593	22.557 ± 0.117	21.092 ± 0.048	20.152 ± 0.031	M, K
587732772665295451.....	180.57622	10.856447	23.182 ± 0.202	22.027 ± 0.107	21.520 ± 0.098	M, K
587732772665295418.....	180.56102	10.852202	23.003 ± 0.188	21.689 ± 0.086	21.076 ± 0.072	M, K
587732772665295407.....	180.55286	10.865665	22.517 ± 0.113	22.271 ± 0.129	22.177 ± 0.171	M, K
587732772665295122.....	180.54705	10.853076	20.925 ± 0.032	20.707 ± 0.036	20.534 ± 0.043	M, K
587732772665294873.....	180.54322	10.860261	18.944 ± 0.009	18.601 ± 0.008	18.474 ± 0.010	M, K

^a Magellan observations.

^b Keck observations.

imaging. We performed photometry using a sample of 10 reference stars (Table 1), six objects in the immediate vicinity of the burst previously identified as stars by the Sloan Digital Sky Survey (SDSS) and four additional objects in the field identified as stars by Henden (2005)¹¹ but also present in SDSS. We use Sloan magnitudes from the SDSS archive¹² of all 10 stars to calibrate our R and I instrumental magnitudes to absolute magnitudes in g' , r' , and i' and then convert back to the Cousins system using the transform equations of Smith et al. (2002).

¹¹ See <ftp://ftp.nofs.navy.mil/pub/outgoing/aah/grb/grb050408.dat>.

¹² See <http://cas.sdss.org/astro/en/tools/search/>.

2.2. Keck Optical Imaging

Keck imaging was acquired through the University of California Target of Opportunity (ToO) program (PI Hurley) on the Keck I 10 m telescope with the dual-beam Low-Resolution Spectrograph Imager (LRIS; Oke et al. 1995). Five 60 s exposures each were taken simultaneously in V and R_c filters (using the D680 dichroic) beginning at 08:11 on 2005 April 11 (2.62 days after the GRB), although because the GRB fell on a chip gap in one V -band exposure only four were used in the final analysis. The co-added R_c -band image is shown in Figure 1. In a 3.3×2.5 field around the transient we matched 46 compact sources in the

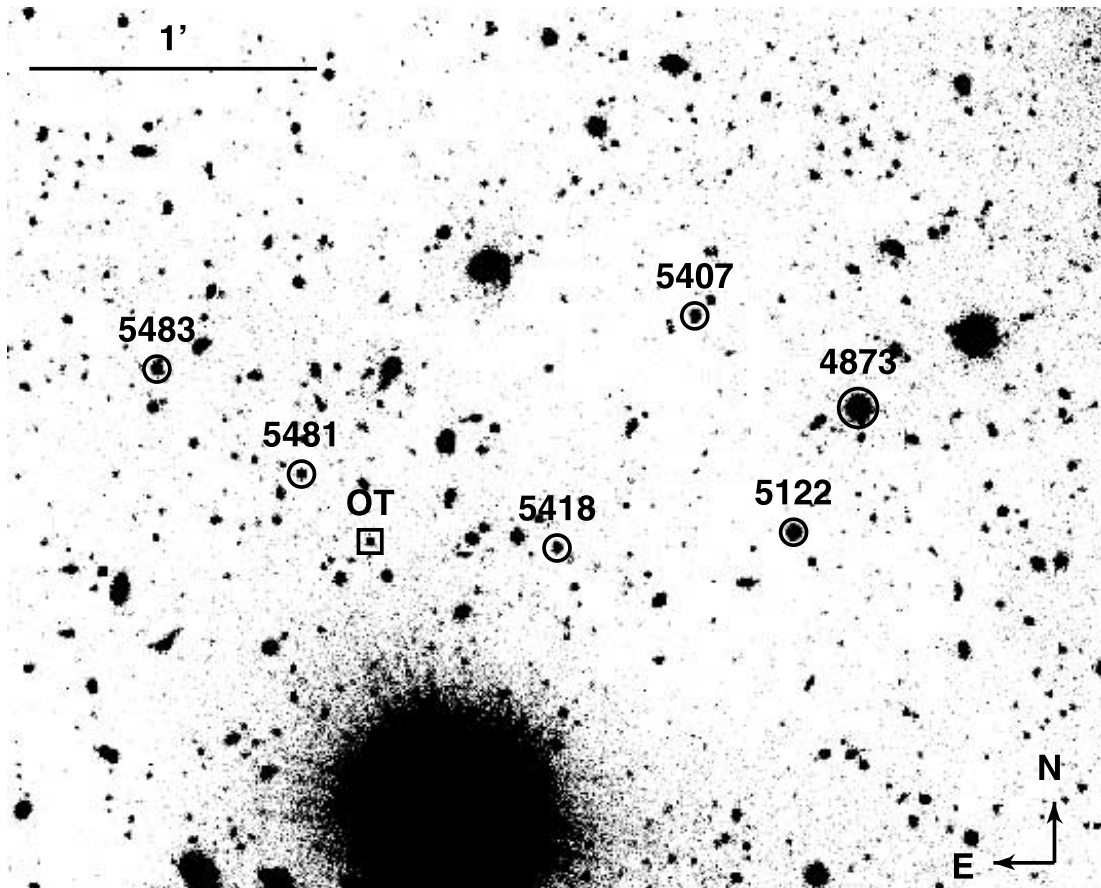


FIG. 1.—Keck V -band image of the field of GRB 050408. The optical transient and nearby reference stars (see Table 1) are marked.

TABLE 2
UVOT *V*-BAND OBSERVATIONS OF GRB 050408

t_{start} (s after Burst)	Exposure (s)	Total Exposure (s)	t_{center} (s)	Limiting Magnitude (3σ) (mag)
2657.1.....	99.77	99.77	2707.0	19.40 ± 0.35
13803.1.....	689.35	689.35	14147.8	20.30 ± 0.25
37264.1.....	380.27	(Combined)
40919.1.....	899.76	1280.03	40130.1	20.82 ± 0.25
59189.1.....	897.35	(Combined)
70765.1.....	899.77	1797.12	64979.0	21.03 ± 0.25

LRIS R_c image with the SDSS catalog in the field and found a position for the optical transient of $\alpha(\text{J2000.0}) = 12^{\text{h}}02^{\text{m}}17^{\text{s}}.301$ and $\delta(\text{J2000.0}) = +10^{\circ}51'09''.10$ with a 1σ uncertainty of 127 and 118 mas in right ascension and declination, respectively.

Photometry on the Keck images was performed using the same procedure as for the Magellan images. Because the imaged field was offset $63''$ south and $5''$ west relative to the Magellan exposure, we used a different sample of Henden stars, but the other six sources used for calibration are the same.

We examined the Keck imaging for the possibility that the host galaxy might be detected by comparing the FWHM of the afterglow with the point-spread functions (PSFs) of field stars. There is no evidence of extension in the afterglow (which, in V band, is at 24th magnitude), limiting the magnitude of the underlying host galaxy. A precise magnitude limit on an extended source is difficult to estimate, but based on the approximate limiting magnitude of faint point sources in the image on which aperture photometry is possible, we limit the magnitude of the host to approximately $I > 25.5$ mag (3σ). In the frame of the host, this corresponds to $M_U > -19$ mag.

2.3. UVOT Reductions

The *Swift* UVOT observed the field of GRB 050408 starting at 17:07 on 2005 April 8, 44.3 minutes after the burst. A series of images were obtained for the GRB field in various filters. An additional 11 batches of UVOT observations were performed for GRB 050408 in the month following the GRB.

Initial results from these observations were reported by the *Swift* UVOT team (Holland et al. 2005). They reported a possible detection ($U = 21.30_{-0.32}^{+0.45}$ mag) in a co-added U -band image with a total exposure time of 2927 s, although they note that the detection is marginal. They also reported no detection in other filters and provided limiting magnitudes for the co-added images. However, the times of the center point of the co-added images were not specified.

We retrieved the UVOT data on GRB 050408 from the *Swift* quick-look archive¹³ and performed photometry using the calibration results and the photometry recipe for *Swift* UVOT from Li et al. (2006). For the U -band data, a careful inspection of all the data combined from the first 2 days after the burst does not convincingly demonstrate the existence of any object down to a limiting magnitude of $U = 21.40$ mag. We also reanalyzed the five V -band exposures from UVOT and found no detections to the limiting magnitudes (3σ) listed in Table 2.

2.4. Infrared Photometry

Infrared imaging of the field of GRB 050408 from both the southern (CTIO) and northern (Mount Hopkins) Two Micron

All Sky Survey (2MASS) 1.3 m telescopes was obtained on the first night of the burst. The ANDICAM¹⁴ instrument mounted on the 1.3 m telescope at Cerro Tololo Inter-American Observatory (CTIO) started observations at 03:15 on 2005 April 9. Images were obtained with a dual-channel camera that allows for simultaneous optical and IR imaging. Both optical and IR images are double-binned in software to give an optical pixel scale of $0''.27 \text{ pixel}^{-1}$ and an IR pixel scale of $0''.37 \text{ pixel}^{-1}$. While standard optical integrations are underway, the ANDICAM instrument allows IR images to be “dithered” by the slight adjustment of three tilt axes of an internal mirror. A combination of six telescope repoints and five internal dithers were used to obtain six separate 360 s I -band images and 30 separate 60 s J -band images per data set.

The Peters Automated Infrared Imaging Telescope (PAIRITEL¹⁵) started observations at April 9 04:03:27, 11.7 hr after the GRB. J -, H -, and K_s -band images were acquired simultaneously with three NICMOS3 arrays in double correlated reads with individual exposure times of 7.8 s. Each image consists of a 256×256 array with a plate scale of $2'' \text{ pixel}^{-1}$. In a given epoch the telescope is dithered every three exposures, allowing for a sky frame appropriate for every image, derived from a star-masked median stack of images before and after, to be created by the pipeline software. The offsets between images are determined by a cross-correlation, and reduced images were then subsampled and stacked with a resolution of $1'' \text{ pixel}^{-1}$. The effective seeing over all the epochs was approximately $2''.3$ FWHM. A stack of all offset-shifted epochs revealed a faint IR source at the location of the optical afterglow.

On the stacked images, we ran SExtractor¹⁶ to find the instrumental magnitudes in a $2''.5$ radius aperture. These magnitudes were used to find an absolute zero-point uncertainty (0.02 mag in all bands), using more than 20 stars in common with the 2MASS catalog in each band. The transient was easily detected and well isolated in H and K_s but was marginally blended in the J . As such, we used the average transient position from the H and K_s image to determine the (x, y) -position in the J -band image. Fixing this center, we used IRAF/PHOT to determine the aperture magnitude (with the 2MASS zero point). For field stars, we confirmed that IRAF/PHOT and SExtractor gave the same results within the errors. The JHK_s magnitudes from PAIRITEL are reported in Table 3.

2.5. Photometry from the Literature

To produce light curves, numerous additional reported measurements were taken from the GCN Circulars. Optical measurements

¹⁴ See <http://www.astronomy.ohio-state.edu/ANDICAM/>; ANDICAM is operated as part of the Small and Moderate Aperture Research Telescope System (SMARTS) consortium (<http://www.astro.yale.edu/smarts/>).

¹⁵ See <http://www.pairitel.org/>.

¹⁶ See <http://sextractor.sourceforge.net/>.

¹³ See <http://swift.gsfc.nasa.gov/cgi-bin/sdc/ql?>.

TABLE 3
OPTICAL/IR OBSERVATIONS OF GRB 050408

Filter	t_{burst} (days)	Magnitude (mag)	Reference	Comments
V.....	0.03133	19.4 ^a	1	UVOT rereduction
	0.16362	20.3 ^a	1	UVOT rereduction
	0.33899	18.5 ^a	2	
	0.40548	21.4	3	
	0.46447	20.82 ^a	1	UVOT rereduction
	0.51747	22.069 ± 0.171	4	
	0.55185	21.7 ^a	3	
	0.63747	22.618 ± 0.191	4	
	0.75297	21.03 ^a	1	UVOT rereduction
	1.60747	23.48 ± 0.612	4	
R.....	2.65673	24.067 ± 0.176	1	Keck
	0.00007	11 ^a	5	
	0.00123	10.9 ^a	5	
	0.00101	16.2 ^a	6	
	0.00416	16.2 ^a	6	
	0.00730	17	6	
	0.01330	19.1 ^a	7	
	0.05983	17.8 ^a	8	
	0.10000	20.4 ± 0.2	9	
	0.12927	20 ^a	10	
	0.15500	21.01 ± 0.07	11	
	0.16122	20.5	12	
	0.18208	21.1 ± 0.05	11	
	0.20083	21.25 ± 0.2	13	
	0.20375	21.25 ± 0.05	11	
	0.22458	21.27 ± 0.05	11	
	0.24125	21.44 ± 0.06	11	
	0.27292	21.37 ± 0.06	11	
	0.28542	21.5 ± 0.06	11	
	0.32580	21.584 ± 0.104	1	Magellan
	0.33899	18.3 ^a	2	
	0.34333	21.64 ± 0.07	11	
	0.36458	21.6 ± 0.07	11	
0.47747	21.888 ± 0.15	4		
0.53622	22.3 ± 0.3	14		
0.57747	21.963 ± 0.129	4		
1.14546	22.55 ± 0.35	15		
5.03250	23.7 ± 0.2	11		
I.....	0.21750	20.4 ± 0.3	14	
	0.32580	21.048 ± 0.123	1	Magellan
	0.33899	17.9 ^a	2	
	0.46930	21.47 ± 0.11	1	CTIO 1.3 m
	0.49747	21.305 ± 0.203	4	
	1.57747	22.288 ± 0.39	4	
Z ^b	2.65673	23.012 ± 0.109	1	Keck
	0.56190	21.8 ± 0.12	16	
J.....	0.33899	18.2 ^a	2	
	0.46885	20.38 ± 0.28	1	CTIO 1.3 m
	0.59837	20.59 ± 0.19	1	PAIRITEL
H.....	0.59837	19.58 ± 0.153	1	PAIRITEL
K.....	0.57962	18.53 ± 0.176	1	PAIRITEL

NOTES.—All optical and NIR observations used in fitting. Data were taken from the GCN circulars and our own observations using Magellan, Keck (LRIS), and PAIRITEL.

^a Upper limit.

^b The NIC-FPS (Near-Infrared Camera and Fabry-Pérot Spectrometer; Vincent et al. 2003) Z was assumed to be equivalent to the SDSS z'.

REFERENCES.—(1) This paper; (2) Melandri et al. 2005; (3) Bayliss et al. 2005; (4) Milne et al. 2005; (5) Tamagawa et al. 2005; (6) Torii 2005; (7) Mizuno et al. 2005; (8) Kuroda et al. 2005; (9) Misra et al. 2005; (10) Klose et al. 2005; (11) Bikmaev et al. 2005; (12) de Ugarte Postigo et al. 2005; (13) Wiersema et al. 2005; (14) Curran et al. 2005; (15) Kahharov et al. 2005; (16) Flasher et al. 2005.

(including upper limits) were retrieved from the circulars in all bands where detections were reported: *B*, *V*, *R*, *I*, *J*, and “Z” (Flasher et al. 2005, interpreted as Sloan z') via GRBLog¹⁷ (Quimby et al. 2004), and the resulting table was screened for errors caused by the automatic parsing of the circulars. We removed duplicate reports, as well as one observation from Milne et al. (2005), which suggested a 1 mag brightening in the *I* band more than 0.5 days after the burst (this was not seen in any other bandpass). We also culled the *B*-band measurement from Milne et al. (2005), which was brighter in flux than simultaneous measurements at longer wavelengths. We replaced data that had been superseded by later analysis for the UVOT limiting magnitudes and Magellan observations, and we added the Keck and PAIRITEL magnitudes. All observations used in our subsequent fitting are listed in Table 3.

3. THE X-RAY AFTERGLOW

The *Swift* XRT (Burrows et al. 2000) began observations of GRB 050408 at 16:34 on 2005 April 8, approximately 672 s after the *HETE-2* trigger (Sakamoto et al. 2005). The XRT operates in a variety of different observing modes, and many were used throughout the observations. Unfortunately, the first 1.8 ks of observations were spent in the “Low Rate Photodiode” mode, which was not useful for this GRB given the faintness of the afterglow. The “Photon Counting” mode observations, which retain full imaging and spectroscopic resolution, began at 17:05:24. As reported by Wells et al. (2005), these XRT data revealed a fading X-ray source in the *HETE-2* error circle. In the ensuing weeks, *Swift* observed the GRB a dozen times. A log of the Photon Counting mode observations is found in Table 4.

We have obtained the XRT data from the *Swift* archive and have analyzed them to determine the temporal and spectral properties of the X-ray afterglow emission. We briefly review the data reduction, and then we discuss the characteristics of the X-ray afterglow.

3.1. *Swift* Data Reduction

Using the Level 1 data from the *Swift* archive, we ran the `xrtpipeline` script packaged with the HEASoft version 6.0 software supplied by the NASA High Energy Astrophysics Science Archive Research Center.¹⁸ We used the default grade selection (grades 0–12) and screening parameters to produce a Level 2 event file recalibrated according to the most current (as of 2005 November 1) calibration files in the *Swift* database.¹⁹ To produce images for source detection, we used the `xselect` software (also part of HEASoft ver. 6.0), with a filter to include only counts in PI channels 30–1000 (corresponding to photon energies of 0.3–10 keV). The PI channel to photon energy conversion was accomplished with the redistribution file `swxpc0t012_20010101v007.rmf` from the calibration database. The effective area of the XRT at the position of the afterglow candidate was determined with the `xrtmkarf` tool, using the correction for a point source.

Although a source extraction region of 20 pixels (47''/2) in radius is recommended in the XRT Data Reduction Guide,²⁰ we chose a smaller extraction region (8 pixels) to mitigate the complications due to a nearby source (designated X1) located about

¹⁷ See <http://grad40.as.utexas.edu/grblog.php>; GRBLog provides a query mechanism for GCN Circulars and their metadata.

¹⁸ See <http://heasarc.gsfc.nasa.gov/>.

¹⁹ See <http://heasarc.gsfc.nasa.gov/docs/heasarc/caldb/swift/>.

²⁰ See http://heasarc.gsfc.nasa.gov/docs/swift/analysis/xrt_swguide_v1_2.pdf.

TABLE 4
Swift XRT APERTURE PHOTOMETRY

Observation	Duration (s)	Exposure (s)	C_A	C_B	Background Count Density (10^{-2} counts pixel $^{-1}$)	GRB Count Rate (10^{-3} counts s $^{-1}$)
1a.....	358.5	358.5	100	2	0.056	396.0 ± 39.7
1b.....	2221.1	2153.8	315	20	0.182	207.4 ± 11.7
1c.....	1385.7	1358.9	130	8	0.084	135.6 ± 11.9
1d.....	1031.2	1025.5	63	6	0.028	87.0 ± 11.0
1e.....	4441.6	1049.7	57	7	0.014	76.9 ± 10.2
1f.....	614.7	536.5	16	1	0.070	42.0 ± 10.6
1g.....	2396.5	409.4	14	1	0.042	48.3 ± 13.0
1h.....	2391.1	287.3	8	1	0.028	39.7 ± 14.0
1i.....	1176.2	332.8	6	1	0.000	25.5 ± 10.5
1j.....	1553.7	429.5	16	1	0.070	52.4 ± 13.3
1k.....	2394.0	659.2	13	1	0.014	27.9 ± 7.8
1l.....	2388.4	639.3	22	5	0.056	48.3 ± 10.5
1m.....	1742.2	437.0	5	2	0.126	15.2 ± 7.3
2.....	52119.8	3399.1	19	2	0.294	7.68 ± 1.83
3.....	80975.1	2828.2	13	6	0.238	6.19 ± 1.82
4.....	59610.9	8361.7	25	10	0.630	3.98 ± 0.85
5.....	29603.5	3116.6	5	5	0.182	2.03 ± 1.02
6.....	180508.6	42828.5	27	80	2.18	0.65 ± 0.17
7.....	82821.9	21278.1	15	48	1.15	0.72 ± 0.26
8.....	86092.9	32161.4	24	51	2.14	0.79 ± 0.22
9.....	87416.5	33091.2	22	59	2.45	0.64 ± 0.20
10.....	35176.6	2943.5	0	12	0.22	...
11.....	133401.7	40145.1	28	120	4.45	0.51 ± 0.19
12.....	167985.7	21764.1	16	50	4.09	0.40 ± 0.26

NOTES.— For each (sub)observation, we list the duration of the XRT observation, the amount of exposure in the Photon Counting mode, the counts in regions A and B (see Fig. 2), the space density of background counts, and the estimate of the GRB count rate using the expression in § 3.1. The count rate uncertainties are 1σ .

$37''.5$ to the north. Although negligible in the early observations, this source can contribute a moderate amount of the flux at the location of the GRB in the late observations. Figure 2 shows $3' \times 3'$ images of the XRT data from the first and eleventh observations. We discuss the regions A and B below.

To quantify the effects of using a smaller extraction region, we used the XRT simulator at the ASI Science Data Center²¹ to investigate the XRT PSF. We simulated a very bright X-ray source

²¹ See <http://www.asdc.asi.it/simulator/swift/>.

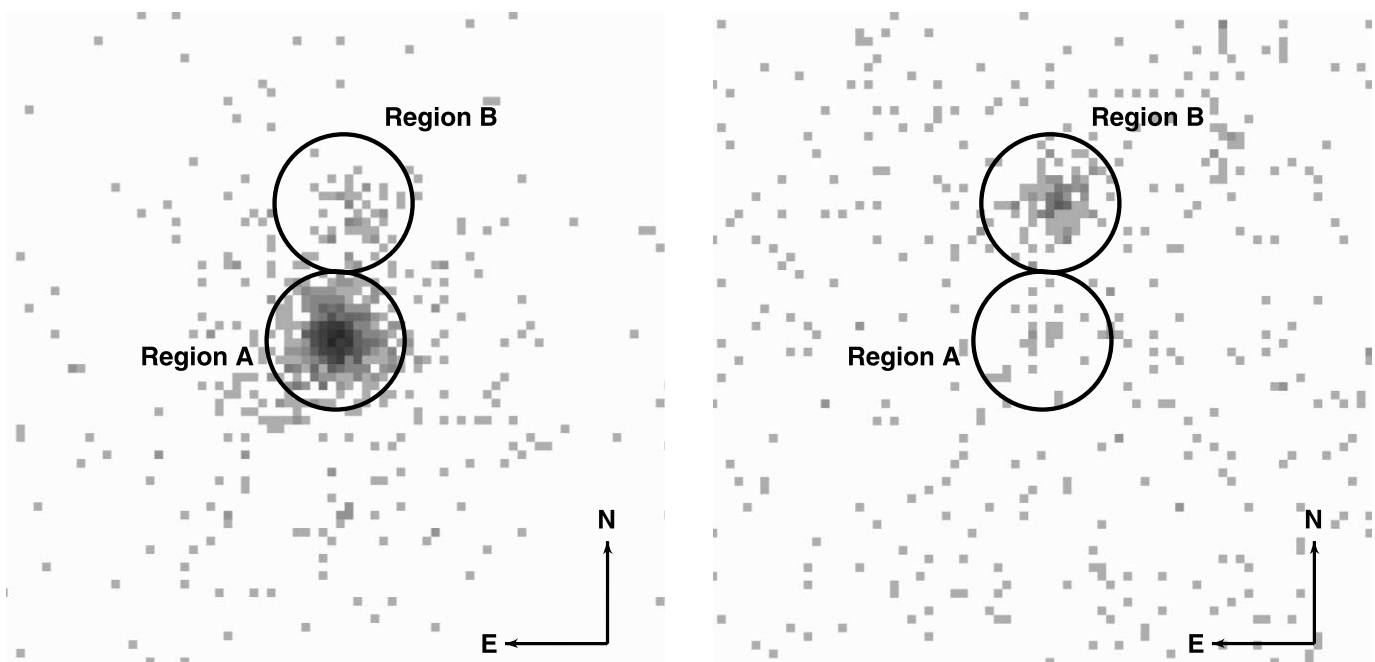


FIG. 2.— Images of the *Swift* XRT data from the first observation (starting at 17:05:24 on 2005 April 8; *left*) and the 11th observation (starting at 02:36:32 on 2005 May 7; *right*). Each image is $3'$ on a side. The extraction regions A (centroid of R.A. = $12^{\text{h}}02^{\text{m}}17^{\text{s}}594$, decl. = $+10^{\circ}51'06''.60$) and B (centroid of R.A. = $12^{\text{h}}02^{\text{m}}17^{\text{s}}448$, decl. = $+10^{\circ}51'44''.06$) are discussed in the text.

TABLE 5
X-RAY SPECTRAL FIT PARAMETERS

Parameter	Before t_{break}	After t_{break}
Photon Index Γ	2.31 ± 0.75	1.33 ± 0.52
$N_{\text{H}}/10^{22} \text{ cm}^{-2}$	$1.5^{+1.1}_{-0.9}$	$0.52^{+0.45}_{-0.20}$

NOTE.—90% confidence intervals.

with a power-law spectrum with a photon index of 1.7 and a column density of $N_{\text{H}} = 10^{20} \text{ cm}^{-2}$. An extraction radius of 20 pixels was found to contain $\sim 90\%$ of the total counts, and an extraction radius of 8 pixels contained $\sim 70\%$ of the total counts. An 8 pixel radius region located $37''5$ from the source position contained $\sim 3\%$ of the total counts.

We can therefore represent the counts (C) in region A as

$$C_A = 0.7C_{\text{GRB}} + 0.03C_{\text{X1}} + C_{\text{bkg}},$$

where C_{bkg} is the number of expected background counts in region A. We use a large, source-free region to the west of the GRB to estimate the background count density in each observation. Using a similar expression for the counts in region B, we can solve for the intrinsic GRB count rate in each observation. We list the relevant quantities for each observation (with the first subdivided into a number of intervals) in Table 4.

3.2. X-Ray Afterglow Spectrum

We investigate the spectral shape of the afterglow emission using a redshifted power-law model with two absorption components—a Milky Way component set at the Galactic value of $N_{\text{H}} = 1.81 \times 10^{20} \text{ cm}^{-2}$ and a redshifted component local to the GRB with N_{H} allowed to vary. We fix the redshift of the power law and the host galaxy absorption at $z = 1.236$.

The spectral fitting was performed in Sherpa (Freeman et al. 2001) with a hybrid Monte Carlo/Levenberg-Marquardt method. We group the data to have at least 15 counts per bin and fit the background-subtracted spectra using χ^2 minimization with Gehrels weighting (Gehrels 1986). To account for the contributions from the source in region B, we fit a power law to the spectrum from this source in observation 11 (which has a relatively strong signal from region B and a weak signal from region A). We include this power law as a fixed component to our model of the GRB spectrum, with a normalization of 3% of the best fit (see § 3.1).

We separately investigate the 0.3–10 keV data before t_{break} (observations 1a and 1b) and after t_{break} (observations 1c–1m, 2–12), where $t_{\text{break}} = 1.26 \times 10^4 \text{ s}$ (see § 4.2), but we find only marginal evidence for differences in the best-fit model parameters, which are listed in Table 5. Figure 3 plots the χ^2 contours as a function of the redshifted power-law photon index Γ and redshifted N_{H} for both sets of data; contours are drawn at 68%, 90%, 95%, and 99%. Our best-fit models had χ^2/dof (degrees of freedom) of 17.2/22 (before t_{break}) and 26.1/30 (after t_{break}).

As the plot shows, the host galaxy column density is poorly constrained and is correlated with the power-law index. The XRT bandpass of 0.3–10 keV corresponds to a rest-frame energy range of 0.67–22.4 keV. Given the low statistical quality of the data and the fact that broadband absorption is most prominent below about 2 keV, it is not surprising that the XRT data do not constrain the column density very well.

We investigate any intrinsic spectral differences before and after t_{break} by considering only data above 2 keV, which are relatively insensitive to the absorbing column to the GRB. We perform a two-sided Kolmogorov-Smirnov test on the energy channel (PI)

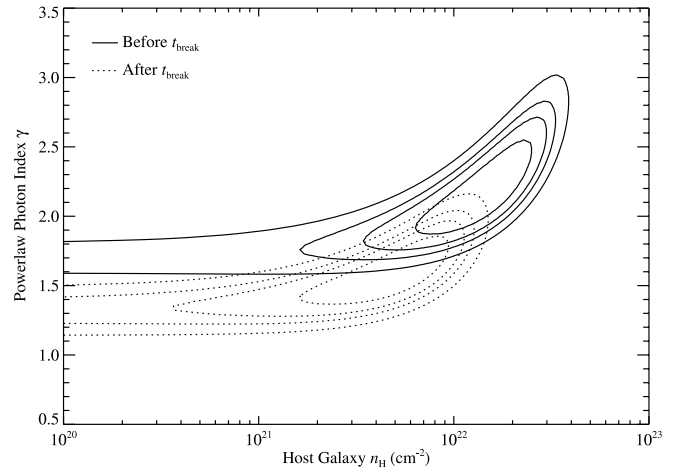


FIG. 3.—The 68%, 90%, 95%, and 99% joint confidence intervals for the power-law photon index of the GRB and the column density of the host galaxy.

cumulative histograms of the data before and after the break. There is only a 0.003 probability that they are drawn from the same parent distribution. To quantify this in terms of a model, we perform a joint fit to the two data sets. The model consists of a simple power law for each spectrum, and the free parameters are the photon index before the break, the difference in photon index from before until after the break, and the normalizations of the power laws. We find an acceptable fit with a χ^2/dof of 11.7/23. For these 2–10 keV data, the best-fit power-law index before t_{break} is 2.3 ± 0.5 , consistent with the best-fit index found from the entire 0.3–10 keV band (Table 5). The difference in spectral index before and after t_{break} is found to be 1.0 ± 0.6 . We plot the minimum χ^2 found as a function of this difference in Figure 4.

To estimate the X-ray flux of the GRB, we use the best-fit model before t_{break} . We need to correct the integrated model flux, since the response files generated by the XRT reduction software assume an extraction radius of 20 pixels, in which 90% of the flux from a point source is contained. Our 8 pixel radius extraction region contains only 70% of the flux from a point source (see § 3.1), so we multiply the best-fit model flux by 1.29. The observed, absorbed flux in the 0.3–10 keV band is $9.0^{+4.4}_{-2.8} \times 10^{-12} \text{ ergs cm}^{-2} \text{ s}^{-1}$. Corrected for Galactic absorption and

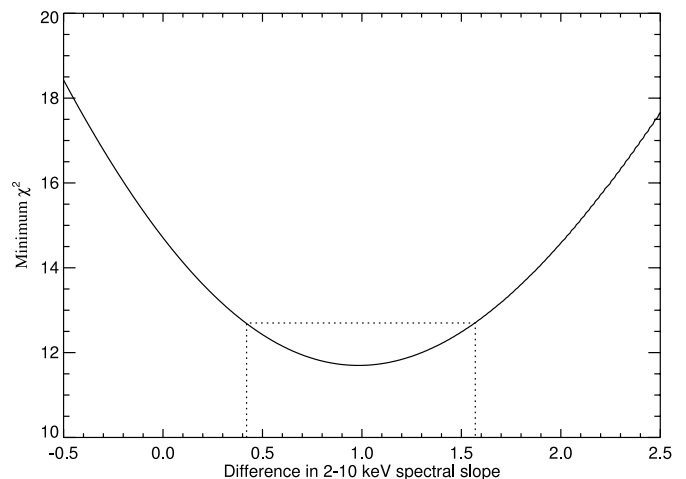


FIG. 4.—Minimum χ^2 value found in a joint spectral fit of the 2–10 keV data before and after t_{break} as a function of the difference in photon indices of the two power-law models. The dotted line corresponds to the 1σ errors.

absorption by the host galaxy, the observed flux is $15.0_{-4.6}^{+7.4} \times 10^{-12}$ ergs cm $^{-2}$ s $^{-1}$. This would correspond to the emitted flux in the 0.67–22.4 keV band. Based on this model, the count rate-to-flux conversion is 38.6×10^{-12} ergs cm $^{-2}$ count $^{-1}$ (absorbed) and 63.7×10^{-12} ergs cm $^{-2}$ count $^{-1}$ (unabsorbed).

4. AFTERGLOW IN THE CONTEXT OF THE SYNCHROTRON SHOCK MODEL

4.1. Optical Afterglow Fitting

We converted the magnitudes in Table 3 to absolute flux densities using zero points from Fukugita et al. (1995) and Cohen et al. (2003), assuming Cousins zero points for all *R*- and *I*-band measurements. We then fit these data in flux-time space with various power-law models of the basic form

$$F = S \left(\frac{t}{t_c} \right)^{-\alpha},$$

where t_c is an arbitrary constant (defined to be 1 day) that sets at what time the measured flux is equal to S . Data without quoted errors were ignored during fitting. We ignore the possible contribution of a constant host galaxy flux to the optical/IR afterglow light: this appears justified by the lack of any extended emission in the latest Keck imaging.

We fit three different models to the data: an unbroken power law where α is constrained to be the same in each filter, an unbroken power law where α is unconstrained, and a broken power law where α and t_{break} are constrained to be the same in each filter. The data, owing largely to the steep decay implied by the *V*-band measurements of Milne et al. (2005), formally prefer a model where the *V*-band decay slope differs from that of the slopes in *R* and *I*. However, a common power law still fits the data well: $\chi^2/\text{dof} = 23.6/24$ (versus 14.7/21 for a variable power law). The broken power-law model offers negligible improvement in χ^2 over an unbroken fit and is excluded to 44% confidence.

If we ignore the peculiar slope of the *V*-band data (physically we do not expect such behavior, and our own measurements do not show a changing spectral index) and look only at the unbroken, common- α model, we derive a best-fit value of $\alpha = 0.789 \pm 0.033$ (see Fig. 5). Using the linear S factors and correcting for Galactic extinction (Schlegel et al. 1998), we then form a simple broadband spectrum (Fig. 6) and fit a simple power law to this as well. This is found to describe the data well ($\chi^2/\text{dof} = 3.19/5$); the resulting value of the spectral index, defined as $F_\nu \propto \nu^{-\beta}$, is then $\beta = 1.30 \pm 0.10$.

Assuming a synchrotron source and certain properties of the medium in the vicinity of the progenitor, these values for the decay constant can be used to calculate p , the electron power spectrum (Sari et al. 1998). The resulting p -values for a homogeneous medium are $p_{\text{lc}} = 1 + 4\alpha/3 = 2.05 \pm 0.04$ (from the light curves) and $p_{\text{bb}} = 2\beta_{\text{bb}} + 1 = 3.61 \pm 0.19$ (from the broadband spectrum). These values are inconsistent and therefore difficult to reconcile with the simplest synchrotron model. As such, we tried to fit a variety of afterglow models in the context of different spectral regimes and external environments.

Following Price et al. (2002), we identify three GRB afterglow models with different predictions about the relationship between the light curve and spectral index: (1) isotropic expansion into a homogeneous medium, (2) isotropic expansion into a wind-stratified medium, and (3) collimated expansion into a homogeneous or wind-stratified medium. The three models share a common form for the relation between these parameters, $\alpha + b\beta + c = 0$, where the values of b and c depend both on the model and on whether the cooling frequency has passed through

the optical and NIR bands of our observations, for a total of six possible closure relations.

For each relation, we calculate the value of the closure parameter $\alpha + b\beta = c$ and its uncertainty, as well as the predicted electron energy spectrum index p , to compare the compatibility of various models to the observations (see Table 6).

All models except the standard model (an isotropic medium with $\nu_c > \nu$) predict a value of $p < 2$, a situation that is unphysical unless there is a high-energy cutoff in the electron energy spectrum. Furthermore, based on the calculated closure parameters, all six relations are excluded with a confidence of at least 4 σ —the spectral index predicted by these models is much less than that observed in our optical and broadband spectra. However, we note that the spectral index is not corrected for host galaxy reddening, which the optical spectrum (discussed in § 5) suggests may be significant.

We examine the effect of extinction by calculating the predicted value for the unextinguished spectral index $\beta = -(\alpha + c)/b$ for each model and fit the observed photometric spectrum for extinction at the host redshift, assuming a value of $R_V = 3.1$. This provides dramatic improvement for all models, with the best fit given by the (equivalent) ISM-R and wind-R models (“R” designating that the cooling frequency is redward of the optical band; i.e., $\nu_c < \nu$), for which $\chi^2/\text{dof} = 5.31/5$. For the standard assumption of $\nu_c > \nu$, we derive a value of $\chi^2/\text{dof} = 7.82/5$ for a homogeneous medium or $\chi^2/\text{dof} = 11.3/5$ for a wind-stratified medium. The jet models do not have an acceptable χ^2/dof whether the cooling frequency is blueward or redward of the optical band. The inferred value of p depends only on α and the model and is not extinction-dependent. As such, only the standard homogeneous-medium model is consistent with an electron energy spectrum that is not cut off at high energies.

Making no assumptions about the unextinguished spectral index and fitting for the best values of β and A_V , the optimum fit is an unextinguished fit: $A_V = 0$ and $\beta = 1.30$, for which $\chi^2/\text{dof} = 3.19/4$. This is not surprising given the data: the observed spectral slope is slightly steeper in the near-IR than in the optical, whereas dust would be expected to steepen the spectral index in the optical more than in the near-IR. However, the data are not inconsistent with the extinguished model: most of the discrepancy is due to the single *K*-band observation.

Confidence contours for fits to the broadband data, varying β and A_V , are shown in Figure 7. From this plot we see the strong covariance between the afterglow spectral index and extinction—and that while a steep-index, low-extinction model is preferred, smaller values of β are also consistent with observations if there is sufficient extinction. Constraining β to the standard model of a homogeneous medium with $\nu_c > \nu$, by which the afterglow is best fit, we find $A_V = 0.57$ mag. While formally the best fit yields $A_V = 0$ mag, the model consistent with the afterglow decay (yielding $A_V = 0.57$ mag) is within 1 σ of the best fit.

If we consider the possibility that R_V may differ substantially from the Galactic value of 3.1, even better fits can be obtained. First, we fit the SMC and LMC values of $R_V = 2.9$ and 2.6, respectively. No improvement in the value of χ^2 is obtained: χ^2/dof increases to 9.0 for the SMC and 10.0 for the LMC extinction laws. However, fitting with R_V as a free parameter, we find remarkable improvement in the fit for large values of R_V : for the case of a constant-density ISM ($\beta = 0.53$) the best-fit χ^2/dof is 1.62/4 (see Fig. 6). This result of a non-Galactic extinction model is 98% significant, according to the F -test.

The best possible fit is one where β , R_V , and A_V are all unconstrained: χ^2/dof improves to 0.83/3. However, this value of β is larger than we would expect from the light curve (under any

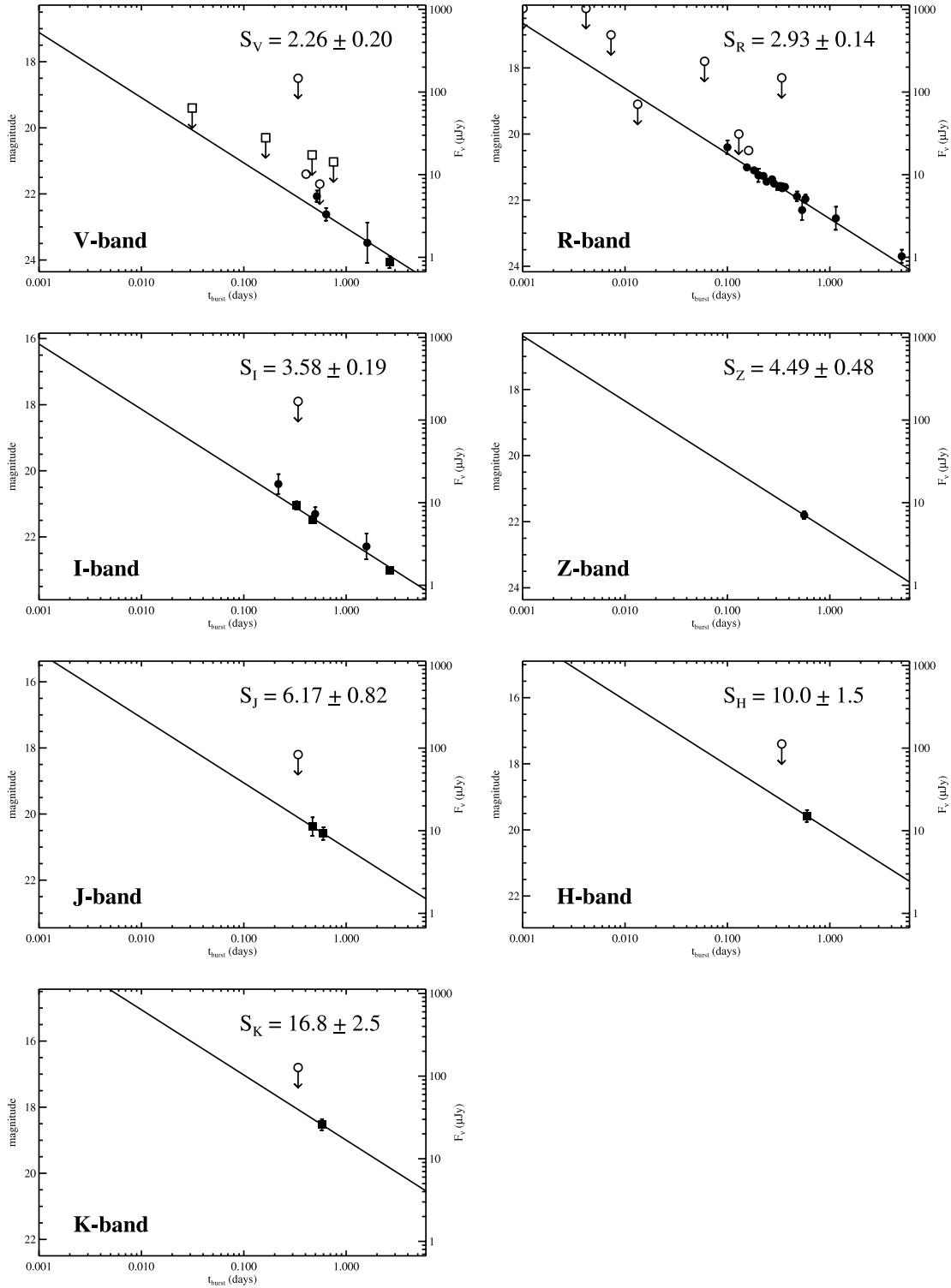


FIG. 5.— *VRIzJHK* light curves of GRB 050408 showing GCN observations (*circles*) and our Keck, Magellan, PAIRITEL, and ANDICAM observations presented in this paper (*squares*). Filled symbols represent detections, while open symbols represent upper limits. The expected flux at $t = 1$ day (before correction for Galactic extinction) in each band is printed at the top right of each plot. The best fit for the decay constant as found in § 4.1 yields $\alpha = 0.789 \pm 0.033$.

established synchrotron-based model), and furthermore this result is only significant at 81% confidence. A summary of the best fits under various assumptions is given in Table 7.

4.2. X-Ray Observations of an Early Light-Curve Break

We attempted to model the GRB count rate with a simple power-law decline in time, but that gave a statistically un-

acceptable fit ($\chi^2/\text{dof} = 51.2/21$, corresponding to a probability of 0.025%). We next tried a broken power-law model of the form

$$R_{x,\text{GRB}}(t) = \begin{cases} At^{-\alpha_{x,1}}, & t \leq t_{\text{break}}, \\ A't^{-\alpha_{x,2}}, & t > t_{\text{break}}, \end{cases}$$

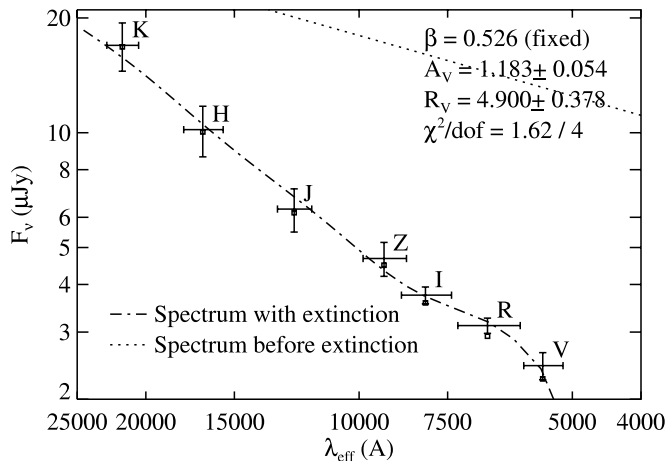


FIG. 6.—Broadband spectrum of the afterglow of GRB 050408 normalized to 1 day after the burst, assuming uniform power-law decay in all bands; β is fixed to the value calculated based on the light curve assuming a homogeneous medium. The data are well fit by a model with $R_V \approx 5$. Other fits are generally not as successful, but the data are (marginally) consistent with a fit using $R_V = 3.1$, $A_V = 0.57$. Fluxes are corrected for Galactic extinction ($A_V = 0.09$). Uncorrected points are shown as small squares for comparison.

where $R_{x,GRB}(t)$ is the GRB X-ray count rate and $A' = A(t_{break})^{\alpha_x, 2 - \alpha_x, 1}$. We performed the model fitting in Sherpa, using a hybrid Monte Carlo/Levenberg-Marquardt optimization method and a χ^2 statistic. This hybrid method randomly samples the parameter space 10,000 times (the Monte Carlo part) for initial values and then uses a Levenberg-Marquardt algorithm to find the local fit statistic minimum nearest to the starting point. Using this method, we found an acceptable fit ($\chi^2/dof = 23.4/19$) whose parameters are listed in Table 8. The data from Table 4 and the best-fit model are plotted in Figure 8. We note that the value of our break parameter $t_{break} = 1.26^{+1.19}_{-0.36} \times 10^4$ s is significantly lower than the value of $(1.2 \pm 0.5) \times 10^5$ s found by Covino et al. (2005). This is most likely due to their fitting algorithm finding a local minimum near this value. Figure 9 plots the minimum χ^2 found as a function of the parameter t_{break} .

5. ABSORPTION SPECTRUM

5.1. Observations and Reductions

An optical spectrum of GRB 050408 was obtained under program GN-2004A-Q-4, a Band 1 rapid ToO program (with carry-over status) executed in the queue at 06:29 on 2005 April 9 using the Gemini North 8 m telescope with GMOS (Hook et al. 2004). We used a $0''.75$ slit, the R831 grating, and the OG515 order-

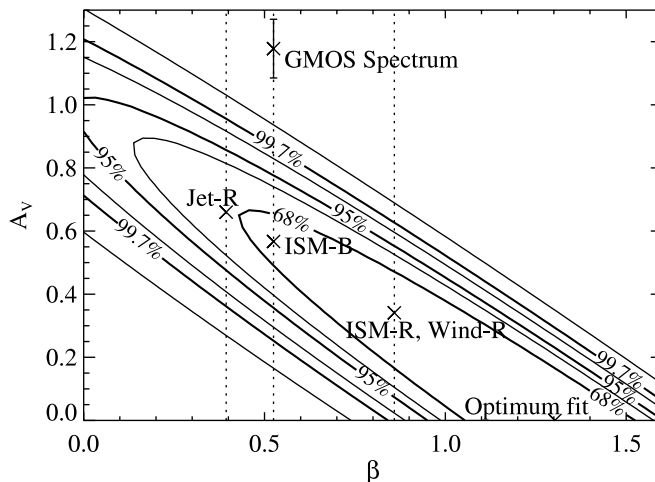


FIG. 7.—The 1, 1.5, 2, 2.5, 3, and 3.5 σ confidence contours for different possible values of the intrinsic β of the afterglow and the host galaxy A_V (assuming $R_V = 3.1$), fitting to the broadband spectrum. In addition, we have overplotted dashed lines corresponding to the values of β predicted from the rate of decay of the light curve assuming various models, and the best-fit value along those lines. Also overplotted is the point inferred from the GMOS spectrum when fit with extinction.

blocking filter and set the central wavelength to 7330 Å. Standard CCD processing and spectrum extraction were accomplished with IRAF using a $1''.16$ aperture. The data were extracted using the optimal algorithm of Horne (1986). Low-order polynomial fits to calibration lamp spectra were used to establish the wavelength scale. Small adjustments derived from night-sky lines in the object frames were applied. Using techniques discussed in Wade & Horne (1988) and Matheson et al. (2000), we employed IRAF and our own IDL routines to flux-calibrate the data and to remove telluric lines using the well-exposed continua of the spectrophotometric standard Feige 34 (Oke 1990).

5.2. Spectral Index and Host Galaxy Dust

Over the small wavelength range of ~ 6280 – 8400 Å, we were able to fit a power-law spectrum to our spectrum of GRB 050408. Correcting only for the Galactic reddening of $A_V = 0.081$ mag (Schlegel et al. 1998), we find $\beta_{spec} = 2.11 \pm 0.29$ and $p_{spec} = 2\beta_{spec} + 1 = 5.22 \pm 0.58$. The errors for these measurements are statistical only. In reality, differential light loss due to the slit position not being at the parallactic angle (Filippenko 1982) and the small wavelength range will contribute additional errors. The p -value derived from the spectrum is statistically inconsistent

TABLE 6
CLOSURE PARAMETERS AND χ^2 FOR DIFFERENT AFTERGLOW MODELS

MODEL	ν_c	[b , c]	CLOSURE	p	FIT WITH EXTINCTION		
					β	A_V	χ^2/dof
ISM	B	[−3/2, 0]	-1.16 ± 0.15	2.05 ± 0.04	0.525	0.567	7.82/5
	R	[−3/2, 1/2]	-0.66 ± 0.15	1.71 ± 0.04	0.859	0.341	5.31/5
Wind.....	B	[−3/2, −1/2]	-1.66 ± 0.15	1.38 ± 0.04	0.192	0.786	11.3/5
	R	[−3/2, 1/2]	-0.66 ± 0.15	1.72 ± 0.04	0.859	0.341	5.31/5
Jet.....	B	[−2, −1]	-2.81 ± 0.20	0.79 ± 0.03	−0.10	0.972	15.3/5
	R	[−2, 0]	-1.81 ± 0.20	0.79 ± 0.03	0.394	0.660	9.05/5

NOTES.—Closure relations and parameters for a variety of afterglow models, after Price et al. (2002). None of the models are well supported by our data without corrections for host extinction. The best-fit χ^2 when fitting for host extinction is given in the rightmost column; much better agreement is achieved.

TABLE 7
 χ^2 FOR DIFFERENT AFTERGLOW AND EXTINCTION MODELS

Extinction Model	Medium	β	R_V	A_V	χ^2/dof
None.....	Unconstrained	1.30	N/A	0*	3.19/5
	ISM	0.53*	N/A	0*	45.0/6
	Wind	0.19*	N/A	0*	77.4/6
Galactic.....	ISM	0.53*	3.1*	0.57	7.8/5
	Wind	0.19*	3.1*	0.79	11.3/5
	Unconstrained	1.30	3.1*	0	3.19/4
SMC.....	ISM	0.53*	2.9*	0.52	8.97/5
LMC.....	ISM	0.53*	2.6*	0.43	10.2/5
Unconstrained.....	ISM	0.53*	4.9	1.18	1.62/4
	Unconstrained	1.05	6.4	0.63	0.83/3

NOTES.—Best-fit parameters and χ^2 for different assumptions about the extinction model (which restricts R_V) and circumburst medium (which restricts β). Asterisks indicate fixed parameters; $\nu < \nu_c$ is assumed.

with that derived from both the broadband spectrum and light-curve decay found in § 4.1, $p_{\text{bb}} = 3.61 \pm 0.19$ and $p_{\text{lc}} = 2.05 \pm 0.044$. However, the p -value derived from the spectrum is much closer to the p_{bb} (within 3σ) than p_{lc} ($>5\sigma$).

As discussed in § 4.1, it is possible that dust in the host galaxy of GRB 050408 is extinguishing the spectrum, causing the deviant spectral shape. We performed our same fitting analysis for the optical spectrum as above, except allowing a dust component at the redshift of the host galaxy. Doing this, we find that an extinction of $A_V = 1.18 \pm 0.09$ mag yields a p -value consistent with that found with the light curve. The best value of $A_V = 1.18$ mag yields $\beta_{\text{spec,dust}} = 0.53 \pm 0.11$ and $p_{\text{spec,dust}} = 2.05 \pm 0.23$. This suggests a significant source of dust in the host galaxy. As shown in § 4.1, the broadband spectrum is consistent with significant host galaxy extinction but not as much as the GMOS spectrum suggests. Again, the discrepancy between these two values is attributed to the small wavelength range of the optical spectrum.

5.3. Absorption-Line Measurements

Figure 10 presents the Ti II, Mg I, Fe I, and [O II] transitions observed in our GMOS spectrum of the afterglow. We have fit a local continuum at the position of each transition and measured the rest equivalent width W_r of each feature (Table 9). The errors only include statistical uncertainty. For the weakest transitions, uncertainty in continuum placement will give an error comparable to the statistical error.

Consider the Ti II measurements first. The W_r values for the four transitions are consistent with the relative oscillator strengths and indicate that the Ti II $\lambda\lambda 3242, 3384$ profiles are saturated. We can place a conservative lower limit to the Ti II column density by adopting the W_r value from Ti II $\lambda 3384$ and ignoring corrections for line saturation. This gives $N_{\text{Ti II}} > 10^{13.2} \text{ cm}^{-2}$. This value is consistent with the column density

TABLE 8
 BROKEN POWER-LAW MODEL PARAMETERS FOR THE XRT

Parameter	Value
$\alpha_{x,1}$	$0.63^{+0.15}_{-0.19}$
$\alpha_{x,2}$	$1.08^{+0.05}_{-0.04}$
t_{break}	$1.26^{+1.19}_{-0.36} \times 10^4 \text{ s}$
A	$59.4^{+160}_{-48.1}$

NOTE.—90% confidence intervals.

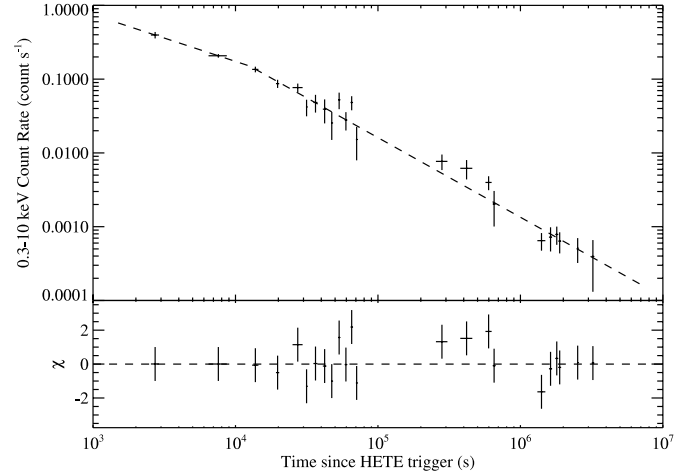


FIG. 8.—GRB X-ray count rate (*crosses*) and best-fitting broken power-law model (*dashed line*). The horizontal bars of the crosses represent the length of the observation interval.

derived from Ti II $\lambda 3230$ assuming that the transition lies on the linear curve of growth.

Both the equivalent width and the implied ionic column density are extraordinary. Although Ti⁺ is the dominant ion in neutral gas, Ti is highly refractory (e.g., Savage & Sembach 1996) and only a trace amount ($\sim 1\%$) is observed in the gas phase of the Milky Way. Therefore, the observed equivalent widths for Ti II $\lambda 3384$ along Milky Way sight lines are $\approx 10 \text{ m}\text{\AA}$ (Pettini et al. 1995; Welsh et al. 1997; Prochaska et al. 2005b), i.e., 50 times smaller than that observed in this GRB afterglow. Even sight lines with $N_{\text{H I}} \sim 10^{22} \text{ cm}^{-2}$ have equivalent widths $W_r < 50 \text{ m}\text{\AA}$ (Welsh et al. 1997). Therefore, the Ti II column density along the sight line through the GRB host galaxy exceeds the largest values observed for the Milky Way by 1 order of magnitude. The few damped Ly α systems with Ti II detections also have rest equivalent widths $< 50 \text{ m}\text{\AA}$ (Dessauges-Zavadsky et al. 2002). Similarly, the LMC has sight lines with equivalent widths $\leq 100 \text{ m}\text{\AA}$ (Caulet & Newell 1996).

Let us now consider the implications for the physical conditions within the ISM of the GRB host galaxy. The gas-phase Ti II column density that one observes is the product of three factors (ignoring ionization corrections): (1) the gas column density

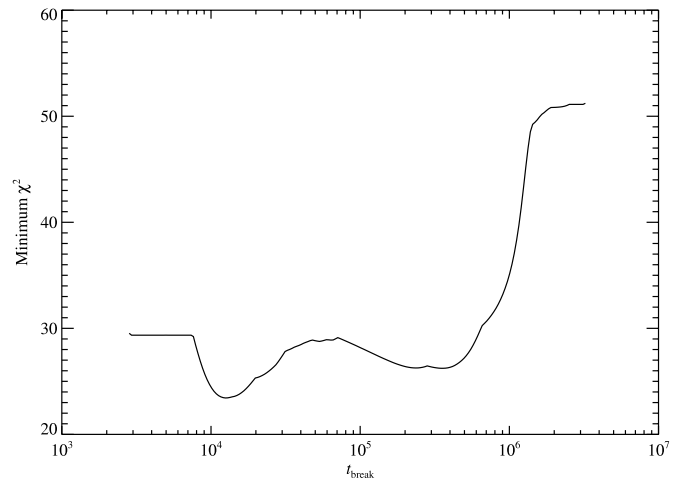


FIG. 9.—Minimum χ^2 value found as a function of t_{break} . The flattening at early and late times is due to the lack of points at these times, making the fit essentially a single power law.

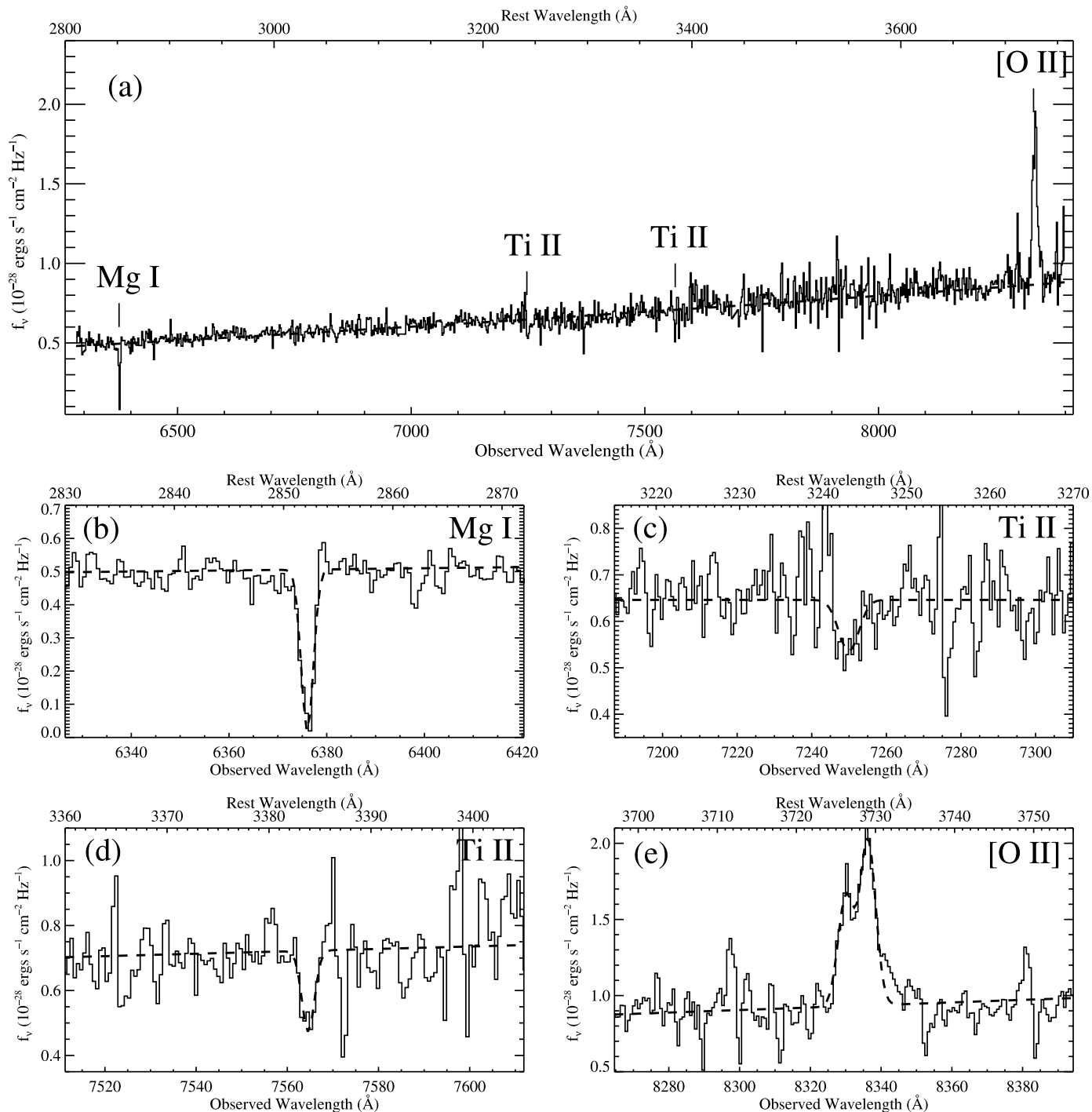


FIG. 10.—Optical spectrum of GRB 050408. (a) Entire spectrum with Ti II, Mg I, and Fe I absorption lines and [O II] emission lines. A power law is fit to the continuum and shown by the dashed line. The power-law fit yields $p_{\text{spec}} = 5.22 \pm 0.58$ without host galaxy reddening and $p_{\text{spec,dust}} = 2.05 \pm 0.23$ if $A_V = 1.18$ in the host galaxy. (b–e) Mg I, Ti II $\lambda 3242$, Ti II $\lambda 3384$, and [O II] transitions in detail, respectively. The dashed lines in these subpanels are Gaussian fits to the lines. The Ti II $\lambda 3242$ line is blended with a bright-sky line at 7245 Å.

$N_{\text{H I}}$, (2) the metallicity of the gas $[\text{Ti}/\text{H}] \equiv \log [N(\text{Ti})/N_{\text{H I}}] - \log [N(\text{Ti})/N_{\text{H I}}]_{\odot}$, and (3) the depletion factor $D_{\text{Ti}} \equiv -\log [N(\text{Ti})_{\text{gas}}/N(\text{Ti})]$; specifically,

$$N(\text{Ti II}) = N_{\text{H I}} + [\text{Ti}/\text{H}] - D_{\text{Ti}} - 7.06,$$

where the constant factor accounts for the solar abundance of Ti (i.e., 12–4.94). The first result is that the gas column density must be large along the afterglow sight line. Even for the unrealistic situation that the gas has solar metallicity and is entirely

undepleted, we have $N_{\text{H I}} > 10^{20.3} \text{ cm}^{-2}$, i.e., the sight line satisfies the H I threshold that defines a damped Ly α system (e.g., Prochaska et al. 2005b). Such a large H I column density is consistent with previous measurements in GRB afterglow spectra (e.g., Vreeswijk et al. 2004). The value implies that the burst originated in a gas-rich and presumably star-forming galaxy.

Second, the fact that GRB 050408 shows a much higher Ti II equivalent width than the Milky Way indicates that $[\text{Ti}/\text{H}] - D_{\text{Ti}}$ is 1 dex higher in the host galaxy. Unless the GRB gas has supersolar metallicity, the observations argue that the gas has a

TABLE 9
ABSORPTION-LINE SUMMARY

Ion	λ_{rest} (\AA)	W_{rest} (m \AA)
Mg I.....	2852.964	1350 ± 70
Ti II.....	3073.877	170 ± 70
	3230.131	200 ± 40
	3242.929	570 ± 80
	3384.740	555 ± 40
Fe I.....	3021.519	300 ± 50

NOTES.—Errors in W_r do not include uncertainty due to continuum placement. For the weakest transitions, the systematic error will be comparable to the statistical error.

significantly lower depletion level than the Milky Way ISM. Interestingly, this result matches the conclusion for several other afterglow spectra (Savaglio & Fall 2004; Vreeswijk et al. 2004; Chen et al. 2005). However, the implied low depletion level contrasts with the strong depletion characteristic of other GRBs (e.g., Savaglio et al. 2003). The lower depletion of Ti could be the result of several factors. First, the dust at high redshift may have a different composition (e.g., much less Ti oxides) than the local universe. Second, the galaxy may be too young for the gas to have been significantly depleted from the gas phase. Third, processes local to the GRB may have resulted in the destruction of the dust grains. These could include UV photodissociation from OB stars in a star-forming region and/or supernova shocks or even a prompt UV flash associated with the GRB event (Waxman & Draine 2000).

To this point, we have restricted the discussion to a comparison of Ti II between GRB 050408 and the Milky Way. Therefore, one might question whether the Milky Way has an unusual Ti depletion level while the characteristics of GRB 050408 are therefore not particularly unique. To investigate this point, we performed the following analysis to further assess the nature of the Ti II detection. First, we compiled the set of strong ($W_r > 1.3 \text{ \AA}$) Mg II systems with absorption redshift $z < 1.8$ identified by Prochter et al. (2006) in the Sloan Digital Sky Survey Data Release 3 quasar sample. These quasar absorption line systems are expected to arise in a variety of environments including galactic disks (Rao & Turnshek 2000), galactic halos (Steidel & Hamilton 1993), and possibly galactic superwinds (Bond et al. 2001). The key point is that the systems were selected to have very strong metal-line Mg II absorption and also strong Fe II absorption, i.e., metal lines with large W_r . We then measured the W_r in a 5 pixel bin centered at the expected positions of Ti II $\lambda\lambda 3242$ and 3384. Of the sample of 4450 Mg II systems, only 120 showed a 3.5σ detection at the position of either Ti II transition. Furthermore, $\frac{2}{3}$ of these “detections” were related to coincidental absorption lines (e.g., Mg II systems at higher redshift) or poorly subtracted sky lines.

Figure 11 plots a histogram of the probable detections for Ti II $\lambda 3384$. Our analysis indicates that fewer than 1% of the sight lines with strong Mg II absorption have correspondingly strong Ti II absorption. Furthermore, only a handful of the positive detections have W_r as large as that of GRB 050408 (<0.1% of all strong Mg II absorbers). It is evident, therefore, that the Ti II absorption observed for GRB 050408 is special to the GRB event.

Finally, consider the observation of Mg I and the possible detection of Fe I. Neither of these ions are dominant in H I regions because their ionization potential is less than 1 ryd. Therefore, it

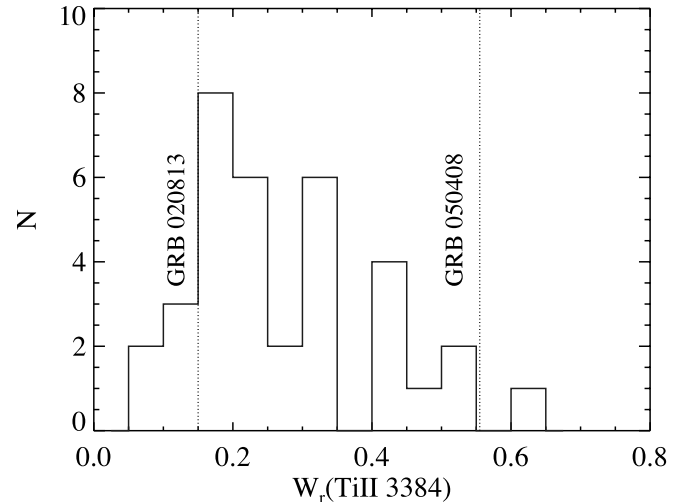


FIG. 11.—Histogram of $W_r(\text{Ti II } \lambda 3384)$ values identified from 4450 strong Mg II systems in SDSS Data Release 3 (Prochter et al. 2006). The observed values in the afterglows of GRB 050408 and 020813 (Fiore et al. 2005) are given by the vertical dotted lines. The figure demonstrates that random sight lines through the universe very rarely penetrate gas with $W_r(\text{Ti II})$ comparable to GRB 050408.

is difficult to infer physical conditions from these features. On the other hand, the strength of Mg I is remarkable. Because the line is highly saturated, its equivalent width gives a lower limit to the velocity width of the gas $\delta v > (W_r/\lambda_r)c > 150 \text{ km s}^{-1}$. We note that the saturated absorption features in the afterglow spectrum of GRB 020813 also indicate a velocity width $\delta v > 200 \text{ km s}^{-1}$ (see also Fiore et al. 2005). This appears to be a common feature of GRB afterglow spectroscopy (Vreeswijk et al. 2004; Ledoux et al. 2005) although not a generic feature (Chen et al. 2005). This is not, however, an expected result in terms of the likely dynamics of the galaxy. For example, assume that the GRB originates near the center of a rotating disk galaxy with circular velocity v_c . The maximum velocity width that one would measure is $\delta v = v_c$ and only for an edge-on sight line. The average value, of course, would be significantly lower. Unless these galaxies are relatively massive—an assertion not supported by their relatively low luminosities (Le Floch et al. 2003)—then the observations suggest an additional velocity field, presumably related to the GRB environment or event.

6. DISCUSSION

6.1. Afterglow Behavior

The synchrotron shock model (Sari et al. 1998) has thus far been very successful at describing afterglow data. The addition of breaks from a reverse shock, a cooling break, and the jet break has further explained several afterglows. However, there are already known inconsistencies with this model.

GRB 030329 has shown several rebrightenings in its optical light curve that cannot be explained by the synchrotron shock model. Suggested explanations for these rebrightenings include the refreshed shock model (Panaitescu et al. 1998; Kumar & Piran 2000).

The current models of GRB afterglows relying on synchrotron radiation from a relativistic shell colliding with an external ISM do not fully explain the afterglow of GRB 050408 without additional considerations, such as host galaxy extinction. The p -value derived from the afterglow decay, $p_{1c} = 2.05 \pm 0.04$, is inconsistent with the p -values derived from the broadband and GMOS spectra, $p_{\text{bb}} = 3.87 \pm 0.20$ and $p_{\text{spec}} = 5.22 \pm 0.58$. The high

p -values derived from the GMOS spectrum are determined from a small wavelength coverage, and the errors on the value are appropriate for the wavelengths shown in the spectrum, but this region of the spectrum may differ significantly from the global spectral shape. With this consideration, we believe that the broadband and GMOS spectra have consistent p -values, which are still inconsistent with the afterglow decay p -value.

The most obvious physical situation that would cause a discrepancy between the afterglow decay and the afterglow spectrum is dust (since the decay should not be affected by this, but the spectrum will be). In § 5, we show that the absorption spectrum is consistent with the afterglow decay if we assume a large ($A_V = 1.18$) host galaxy extinction. This value is somewhat larger than that from the broadband spectrum ($A_V = 0.567 \pm 0.044$, assuming $R_V = 3.1$), but this is not surprising given the discrepancy between the observed spectra. If we allow A_V and R_V to vary, we find that $A_V = 1.18$ with $R_V = 4.9$. This value for R_V is similar to that of molecular clouds (Valencic et al. 2004).

The break observed in the X-ray afterglow is intriguing. This change from a shallow ($0.2 < \alpha < 0.8$) to slightly steeper ($1 < \alpha < 1.5$) power-law index has been very common in *Swift* bursts (Nousek et al. 2006). Although the break may be associated with a physical mechanism associated with the afterglow (such as a minimum frequency break), other possibilities include energy reinjection. Our lack of excellent sampling near the time of the break and the overall low X-ray flux do not allow us to make further predictions.

6.2. Hydrogen Column and Ti II Abundance

From § 3.1, we found that the amount of N_H found by fitting the X-ray spectrum is $N_{H1} \approx 10^{22} \text{ cm}^{-2}$. Examining the optical absorption spectrum in § 5, we found $N_{H1} > 10^{20.3} \text{ cm}^{-2}$. The large equivalent widths associated with Ti II in our absorption spectrum of GRB 050408 suggest a large hydrogen column, a supersolar metallicity, and/or a lower Ti depletion than the Milky Way. A supersolar metallicity seems unlikely given the redshift of the galaxy of $z = 1.236$. We are then forced to look at the hydrogen column and Ti depletion. If there is any depletion of Ti or if the Ti/H ratio is subsolar in the host galaxy, both of which are likely, then a value of $N_{H1} \approx 10^{22} \text{ cm}^{-2}$ is quite reasonable.

The strong Ti II lines are an interesting feature. Ti II lines as strong as those in the afterglow of GRB 050408 are very rare in Mg I absorption systems ($\sim 0.1\%$). However, these lines are present in other GRB afterglow spectra. This indicates that the physical properties of the environment of these GRBs that create the strong lines are linked to the GRB progenitor formation or the GRB progenitor-affected environment. It appears that a low Ti depletion is somehow linked to the formation of massive stars, the environment created around such massive stars, or perhaps the event itself.

6.3. Line Velocities

The large velocities ($v \approx 150 \text{ km s}^{-1}$) implied by the absorption lines in the spectrum of GRB 050408 are not easily explained by the kinematics of the host galaxy. Although it is possible that the host is a very massive galaxy (although unlikely considering the luminosity of $M_V > -18$), another scenario is that the velocity is local to the GRB. The presumed progenitors to long-duration GRBs, Wolf-Rayet stars, are known to have large winds and, therefore, large line velocities associated with them (Gull et al. 2005). Mirabal et al. (2003) saw distinct systems of lines offset by ~ 450 , ~ 1000 , and $> 1000 \text{ km s}^{-1}$ from the host redshift, which they interpreted as a shell nebula from a Wolf-

Rayet progenitor surrounding the GRB. The resolution of our spectrum is too low to see distinct components within our lines; however, we can safely say that there is no strong, distinct component at $\sim 3000 \text{ km s}^{-1}$ relative to the host galaxy.

6.4. Progenitor Environment

The combination of several observables suggests that the GRB occurred in a star-forming environment, perhaps a molecular cloud. The large line velocities measured in the spectrum are unlikely to have been caused by galactic rotation and are most likely caused by the motion of gas in the local progenitor environment. The large value for R_V is also suggestive of a dense environment, perhaps as dense as a molecular cloud. These observations support the collapsar scenario that predicts that the progenitors of long-duration GRBs are massive stars, which explode in situ.

7. CONCLUSIONS

GRB 050408 is a particularly interesting object both showing the consistency of predicted models and showing new and extreme cases of physical phenomena. In particular, we have shown:

1. The synchrotron electrons had energy index of $p \approx 2$, the lower limit of physically acceptable systems (Mészáros & Rees 1997; Sari et al. 1998). This is supported directly by the optical-NIR afterglow decay and the X-ray spectrum. There is also indirect support (assuming particular models) from the optical spectrum, the optical-NIR broadband spectrum, and the X-ray afterglow decay.

2. The X-ray afterglow shows a break at $1.26 \times 10^4 \text{ s}$ after the burst. This break is not attributed to a jet break. One possible explanation is continued energy injection.

3. The hydrogen column is very large ($N_{H1} \approx 10^{22} \text{ cm}^{-2}$). The optical spectrum also showed one of the most extreme Ti absorption systems observed. The combination of these facts suggests that there is an incredibly low amount of Ti depletion in the environment of GRB 050408. This has been noted for other GRBs, suggesting that low Ti depletion is linked to GRB environments, possibly due to high-mass star formation, the environments of newly formed supernova and GRB remnants, or dust destruction from the GRB.

4. The large velocities associated with the absorption lines are not easily explained by the kinematics of the host galaxy. For a systemic velocity of $v \approx 150 \text{ km s}^{-1}$, a large mass (and possibly a special geometry) is needed. However, we have shown that the host of GRB 050408 is faint $M_U > -19$, comparable to the LMC. This suggests that the velocities originate close to the progenitor, from either a wind from the Wolf-Rayet progenitor star or older supernova explosions close to the progenitor.

We are grateful to the Gemini observing staff. This work is based on observations obtained at the Gemini Observatory, which is operated by the Association of Universities for Research in Astronomy, Inc., under a cooperative agreement with the NSF on behalf of the Gemini partnership: the National Science Foundation (US), the Particle Physics and Astronomy Research Council (UK), the National Research Council (Canada), CONICYT (Chile), the Australian Research Council (Australia), CNPq (Brazil), and CONICET (Argentina). J. S. B., J. X. P., and H.-W. C. are partially supported by a grant from the NASA Swift Guest Investigator Program. D. P. gratefully acknowledges support provided by NASA through Chandra Postdoctoral Fellowship

grant No. PF4-50035 awarded by the Chandra X-Ray Center, which is operated by the Smithsonian Astrophysical Observatory for NASA under contract NAS8-03060. G. A., M. K., and S. P. are supported in part by the US Department of Energy under contract DE-AC03-76SF000098. The Peters Automated Infrared Imaging Telescope (PAIRITEL) is operated by the Smithsonian Astrophysical Observatory (SAO) and was made possible by a grant from the Harvard University Milton Fund, the camera loan from the University of Virginia, and the continued support of the

SAO and UC Berkeley. R. J. F. would like to thank Thomas Matheson for his assistance with the GMOS data reduction. R. J. F. would also like to especially thank Steve Dawson for showing examples of complicated figures and for being a great example of a successful and universally admired astronomer. The authors wish to extend special thanks to those of Hawaiian ancestry on whose sacred mountain we are privileged to be guests. Without their generous hospitality, many of the observations presented herein would not have been possible.

REFERENCES

- Bayliss, M., Nysewander, M., Haislip, J., Crain, J. A., Foster, A., Kirschbrown, J., MacLeod, C., & Reichart, D. 2005, GCN Circ. 3228, <http://gcn.gsfc.nasa.gov/gcn3/3228.gcn3>
- Berger, E., Gladders, M., & Oemler, G. 2005, GCN Circ. 3201, <http://gcn.gsfc.nasa.gov/gcn3/3201.gcn3>
- Bigelow, B. C., Dressler, A. M., Shectman, S. A., & Epps, H. W. 1998, Proc. SPIE, 3355, 225
- Bikmaev, I., et al. 2005, GCN Circ. 3262, <http://gcn.gsfc.nasa.gov/gcn3/3262.gcn3>
- Bond, N. A., Churchill, C. W., Charlton, J. C., & Vogt, S. S. 2001, ApJ, 562, 641
- Burrows, D. N., et al. 2000, Proc. SPIE, 4140, 64
- Capalbi, M., Romano, P., Mangano, V., Godet, O., Angelini, L., & Burrows, D. N. 2005, GCN Circ. 3254, <http://gcn.gsfc.nasa.gov/gcn3/3254.gcn3>
- Caulet, A., & Newell, R. 1996, ApJ, 465, 205
- Chen, H.-W., Prochaska, J. X., Bloom, J. S., & Thompson, I. B. 2005, ApJ, 634, L25
- Cohen, M., Wheaton, W. A., & Megeath, S. T. 2003, AJ, 126, 1090
- Covino, S., Capalbi, M., Perri, M., Mangano, V., & Burrows, D. N. 2005, GCN Circ. 3508, <http://gcn.gsfc.nasa.gov/gcn3/3508.gcn3>
- Curran, P., et al. 2005, GCN Circ. 3211, <http://gcn.gsfc.nasa.gov/gcn3/3211.gcn3>
- de Ugarte Postigo, A., et al. 2005, GCN Circ. 3192, <http://gcn.gsfc.nasa.gov/gcn3/3192.gcn3>
- Dessauges-Zavadsky, M., Prochaska, J. X., & D'Odorico, S. 2002, A&A, 391, 801
- Filippenko, A. V. 1982, PASP, 94, 715
- Fiore, F., et al. 2005, ApJ, 624, 853
- Flasher, J., et al. 2005, GCN Circ. 3561, <http://gcn.gsfc.nasa.gov/gcn3/3561.gcn3>
- Freeman, P., Doe, S., & Siemiginowska, A. 2001, Proc. SPIE, 4477, 76
- Fukugita, M., Shimasaku, K., & Ichikawa, T. 1995, PASP, 107, 945
- Gehrels, N. 1986, ApJ, 303, 336
- Gehrels, N., et al. 2004, ApJ, 611, 1005
- Godet, O., et al. 2005, GCN Circ. 3222, <http://gcn.gsfc.nasa.gov/gcn3/3222.gcn3>
- Gull, T. R., Vieira, G., Bruhweiler, F., Nielsen, K. E., Verner, E., & Danks, A. 2005, ApJ, 620, 442
- Henden, A. 2005, GCN Circ. 3454, <http://gcn.gsfc.nasa.gov/gcn3/3454.gcn3>
- Holland, S. T., et al. 2005, GCN Circ. 3227, <http://gcn.gsfc.nasa.gov/gcn3/3227.gcn3>
- Hook, I. M., Jørgensen, I., Allington-Smith, J. R., Davies, R. L., Metcalfe, N., Murowinski, R. G., & Crampton, D. 2004, PASP, 116, 425
- Horne, K. 1986, PASP, 98, 609
- Kahharov, B., Ibrahimov, M., Sharapov, D., Pozanenko, A., Rumyantsev, V., & Beskin, G. 2005, GCN Circ. 3261, <http://gcn.gsfc.nasa.gov/gcn3/3261.gcn3>
- Klose, S., Laux, U., Stecklum, B., & Greiner, J. 2005, GCN Circ. 3194, <http://gcn.gsfc.nasa.gov/gcn3/3194.gcn3>
- Kumar, P., & Piran, T. 2000, ApJ, 535, 152
- Kuroda, D., Yanagisawa, K., & Kawai, N. 2005, GCN Circ. 3195, <http://gcn.gsfc.nasa.gov/gcn3/3195.gcn3>
- Ledoux, C., et al. 2005, GCN Circ. 3860, <http://gcn.gsfc.nasa.gov/gcn3/3860.gcn3>
- Le Floc'h, E., et al. 2003, A&A, 400, 499
- Li, W., Jha, S., Filippenko, A. V., Bloom, J. S., Pooley, D., Foley, R. J., & Perley, D. A. 2006, PASP, 118, 37
- Matheson, T., Filippenko, A. V., Ho, L. C., Barth, A. J., & Leonard, D. C. 2000, AJ, 120, 1499
- Melandri, A., et al. 2005, GCN Circ. 3205, <http://gcn.gsfc.nasa.gov/gcn3/3205.gcn3>
- Mészáros, P., & Rees, M. J. 1997, ApJ, 476, 232
- Milne, P. A., Williams, G. G., & Park, H.-S. 2005, GCN Circ. 3258, <http://gcn.gsfc.nasa.gov/gcn3/3258.gcn3>
- Mirabal, N., et al. 2003, ApJ, 595, 935
- Misra, K., Pandey, S. B., & Kamble, A. P. 2005, GCN Circ. 3202, <http://gcn.gsfc.nasa.gov/gcn3/3202.gcn3>
- Mizuno, T., Arai, Y., Yamagishi, H., Soyano, T., Urata, Y., Tamagawa, T., & Huang, K. Y. 2005, GCN Circ. 3207, <http://gcn.gsfc.nasa.gov/gcn3/3207.gcn3>
- Nousek, J. A., et al. 2006, ApJ, 642, 389
- Oke, J. B. 1990, AJ, 99, 1621
- Oke, J. B., et al. 1995, PASP, 107, 375
- Panaitescu, A., Mészáros, P., & Rees, M. J. 1998, ApJ, 503, 314
- Pettini, M., Lipman, K., & Hunstead, R. W. 1995, ApJ, 451, 100
- Price, P. A., et al. 2002, ApJ, 572, L51
- Prochaska, J. X., Bloom, J. S., Chen, H.-W., Foley, R. J., & Roth, K. 2005a, GCN Circ. 3204, <http://gcn.gsfc.nasa.gov/gcn3/3204.gcn3>
- Prochaska, J. X., Herbert-Fort, S., & Wolfe, A. M. 2005b, ApJ, 635, 123
- Prochter, G. E., Prochaska, J. X., & Burles, S. 2006, ApJ, 639, 766
- Quimby, R., McMahon, E., & Murphy, J. 2004, in AIP Conf. Proc. 727, Gamma-Ray Bursts: 30 Years of Discovery, ed. E. E. Fenimore & M. Galassi (Melville: AIP), 529
- Rao, S. M., & Turnshek, D. A. 2000, ApJS, 130, 1
- Sakamoto, T., et al. 2005, GCN Circ. 3189, <http://gcn.gsfc.nasa.gov/gcn3/3189.gcn3>
- Sari, R., Piran, T., & Narayan, R. 1998, ApJ, 497, L17
- Savage, B. D., & Sembach, K. R. 1996, ARA&A, 34, 279
- Savaglio, S., & Fall, S. M. 2004, ApJ, 614, 293
- Savaglio, S., Fall, S. M., & Fiore, F. 2003, ApJ, 585, 638
- Schlegel, D. J., Finkbeiner, D. P., & Davis, M. 1998, ApJ, 500, 525
- Smith, J. A., et al. 2002, AJ, 123, 2121
- Soderberg, A. M. 2005, GCN Circ. 3234, <http://gcn.gsfc.nasa.gov/gcn3/3234.gcn3>
- Steidel, C. C., & Hamilton, D. 1993, AJ, 105, 2017
- Tamagawa, T., Urata, Y., Usui, F., Onda, K., Abe, K., & Tashiro, M. 2005, GCN Circ. 3214, <http://gcn.gsfc.nasa.gov/gcn3/3214.gcn3>
- Torii, K. 2005, GCN Circ. 3232, <http://gcn.gsfc.nasa.gov/gcn3/3232.gcn3>
- Valencic, L. A., Clayton, G. C., & Gordon, K. D. 2004, ApJ, 616, 912
- Vincent, M. B., et al. 2003, Proc. SPIE, 4841, 367
- Vreeswijk, P. M., et al. 2004, A&A, 419, 927
- Wade, R. A., & Horne, K. 1988, ApJ, 324, 411
- Waxman, E., & Draine, B. T. 2000, ApJ, 537, 796
- Wells, A. A., et al. 2005, GCN Circ. 3191, <http://gcn.gsfc.nasa.gov/gcn3/3191.gcn3>
- Welsh, B. Y., Sasseen, T., Craig, N., Jelinsky, S., & Albert, C. E. 1997, ApJS, 112, 507
- Wiersema, K., et al. 2005, GCN Circ. 3200, <http://gcn.gsfc.nasa.gov/gcn3/3200.gcn3>